# Dynamical mode coexistence and chaos in a nanogap spin Hall nano-oscillator

Lina Chen,[1,2] Kaiyuan Zhou,[1,2] S. Urazhdin,[3] Wencong Jiang,[1] Y. W. Du,[1] and R. H. Liu[1,2,3]

[1]*National Laboratory of Solid State Microstructures, School of Physics and Collaborative Innovation Center of Advanced Microstructures, Nanjing University, Nanjing 210093, China*

[2]*Shenzhen Research Institute of Nanjing University, Shenzhen 570126, China*

[3]*Department of Physics, Emory University, Atlanta, Georgia 30322, USA*

(Received 10 June 2019; revised manuscript received 11 August 2019; published 27 September 2019)

We utilize microwave spectroscopy to study the auto-oscillation modes in the nanogap spin Hall nano-oscillators based on Permalloy/Pt bilayers. We show that two distinct spin-wave modes appear in such oscillators, regardless of the magnetic film thicknesses or the size of the electrode gap. We identify the primary mode as a nonlinear self-localized bullet soliton localized at the center of the gap between the electrodes, which is excited over a broad range of currents, field magnitudes, and orientations. The secondary high-frequency mode appears at higher currents and coexists with the primary bullet mode. Micromagnetic modeling shows that this mode is stabilized by the dipolar field of the bullet, and its spatial profile exhibits two maxima offset from the center of the gap in two opposite directions collinear with the field. Simulations also suggest chaotic dynamics that emerges at large currents due to the incoherent coupling between the two modes. Our results demonstrate the possibility to induce and control complex nonlinear dynamical phenomena in spin Hall oscillators, which can be utilized in the emergent neuromorphic and reservoir computing applications.

DOI: 10.1103/PhysRevB.100.104436

## I. INTRODUCTION

Spin-polarized electric currents generated, for example, by spin filtering in spin valves or by spin-dependent tunneling in magnetic tunneling junctions, can be utilized to control the configuration of nanomagnetic systems, and are thus essential for the operation of active spin-based electronic (spintronic) devices such as spin-torque magnetoresistive random-access memory and magnetic nano-oscillators [1–4]. Traditional active spintronic devices included a ferromagnetic (F) layer traversed by the current to generate spin polarization [3,4], which resulted in significant Joule heating. Recent experimental studies have demonstrated that nonmagnetic materials with large spin-orbit interaction, such as heavy metals and topological materials (Ns), can provide an efficient alternative approach [5–9]. In such devices, some combination of pure spin current induced by the spin Hall effect (SHE) inside the N material, and the current-induced Rashba effect at its interface, can result in a significant torque exerted on the magnetization of an adjacent F. This mechanism does not require the charge current to flow through F, minimizing its Joule heating, and enabling one to use electrically insulating low-loss magnetic materials [10–12]. Very large achievable spin Hall angles [13] can result in efficient charge to spin current conversion, not limited by the value of electron's spin.

Decoupling of the spin from charge current enabled by SHE has provided unprecedented geometric and structural flexibility, leading to the development of a variety of SHE-based device designs. Among such devices, spin Hall nano-oscillators (SHNOs)—devices that generate microwaves due to the auto oscillation of magnetization induced by spin current—have particularly benefited from such flexibility, due to the direct relation between the spectral and the spatial characteristics of the dynamical magnetization states. Various combinations of materials and geometries have been investigated, including triangular nanogap contacts on extended magnetic films [14–22], nanoconstrictions, and nanowires [23–27]. These devices have been characterized by multiple techniques, including micro-focus Brillouin light scattering (BLS) [14], microwave spectroscopy, time-resolved scanning Kerr microscopy [28], and micromagnetic simulations [29–31].

For SHNO based on in-plane magnetized films locally excited by spin current, the nonlinear theory of magnetization dynamics predicts that the generated spin waves with finite group velocities are efficiently damped out due to their radiation away from the excitation region. Meanwhile, the lowest-frequency mode characterized by zero group velocity becomes locally nonlinearly redshifted by the excitation, resulting in the formation of self-localized bullet oscillation mode, with the frequency below the spectrum of linear spin-wave modes [14,32]. Spatially resolved BLS measurements have indeed shown that the oscillation is localized to an approximately 100 nm region, with auto-oscillation frequency lying significantly below that of the ferromagnetic resonance (FMR) [14]. However, the limited spectral resolution of BLS did not allow one to analyze the dynamical coherence of the oscillation or determine whether only a single mode or multiple modes were involved.

Multiple linear and nonlinear spin-wave modes can exist in SHNO [1]. Indeed, microwave spectroscopy revealed a significant complexity of the dynamical states excited by spin current [15,16,19,24,27]. However, these measurements have not yet yielded a consistent picture of the nature of the dynamical modes involved in the auto oscillation or approaches to controlling them, which is necessary for the

 

development of SHNO-based coherent microwave sources, efficiently synchronizing the devices to external signals or other SHNO, and for the neuromorphic applications relying on the complex nonlinear dynamical states.

Here, we utilize microwave spectroscopy to study the dynamical modes excited by spin current in planar nanogap SHNO based on Permalloy (Py)/Pt bilayers. We analyze the dependence on current $I$, the magnitude of the external field $H$, and the angle $\theta$ it forms with the direction of the current flow, for three representative devices with different thicknesses of the magnetic Py layer and the size of the gap between the electrodes. We identify several common features of the dynamical behaviors in SHNO, which are robust with respect to the variations of the direction and magnitude of the magnetic field. A single mode is excited at small currents over a large range of experimental parameters. An additional higher-frequency dynamical mode that coexists with the primary mode emerges at larger currents. With further current increase, the auto oscillation transitions to a new dynamical regime characterized by very broad spectral features. To elucidate the observed behaviors, we perform micromagnetic simulations of spin-current-induced magnetization dynamics in the studied SHNOs. The results of the simulations qualitatively reproduce our data and provide insight into the spatial characteristics of the observed dynamical states. The primary auto-oscillation mode is identified as the nonlinear spin-wave bullet localized at the center of the electrode gap. Its approximately elliptical spatial profile is elongated in the direction of the total field $H_{\rm tot}$. The secondary mode is also localized. Its spatial profile is characterized by two maxima offset from the device center in two opposite directions collinear with the field. The formation of this mode can be attributed to the spatially inhomogeneous dipolar field produced by the primary bullet mode. The coexistence of the two modes is facilitated by their spatial separation, while their dynamic coupling causes chaotic magnetization dynamics at large currents. Our findings suggest the possibility of controllable dynamical redistribution of the oscillation energy between dynamical modes, driven by external signals, parameter modulation, and/or by coupling to other SHNO. Controllable nonlinear dynamical behaviors can be utilized for the development of SHNO networks with neuromorphic functionalities.

## II. EXPERIMENT

### A. Device fabrication and measurement setup

The devices were based on Pt/Py bilayers, deposited on sapphire substrates by magnetron sputtering at room temperature. One of the tested SHNOs, labeled device No. 1, was based on a Py(5)/Pt(4) bilayer, while the other two, labeled devices No. 2 and No. 3, were based on the Py(3)/Pt(2) bilayers. All thicknesses are given in nanometers. The bilayers were pattered by e-beam lithography into circular disks with a 4$\mu$m diameter, with two pointed Au(100) electrodes fabricated on top of the bilayer [Fig. 1(a)]. The separation between the endpoints of the Au electrodes was 65 nm for device No. 1, 80 nm for device No. 2, and 70 nm for device No. 3, as determined by scanning electron microscopy. An in-plane electrical current applied to the Au electrodes flowed through the Py/Pt bilayer mostly in the region localized between the electrode tips, due to the significantly larger sheet resistance of the bilayer compared to that of the Au electrodes. A combination of the SHE in Pt and the Rashba effect at the Py/Pt interface produced a spin-orbit torque on the Py magnetization [33,34]. The resulting auto oscillation of the Py magnetization was detected as a microwave-frequency voltage, which was produced by the current flowing through the Py layer due to its resistance oscillations associated with the anisotropic magnetoresistance (AMR) effect. Measurements were performed at the experimental temperature of 6 K to minimize thermal spectral broadening, with the magnetic field $H$ applied in the film plane at a variable angle $\theta$ relative to the direction of current flow.

### B. Current-driven dynamical modes

Figure 1(b) shows a pseudocolor map of the representative current dependence of the microwave power spectral density

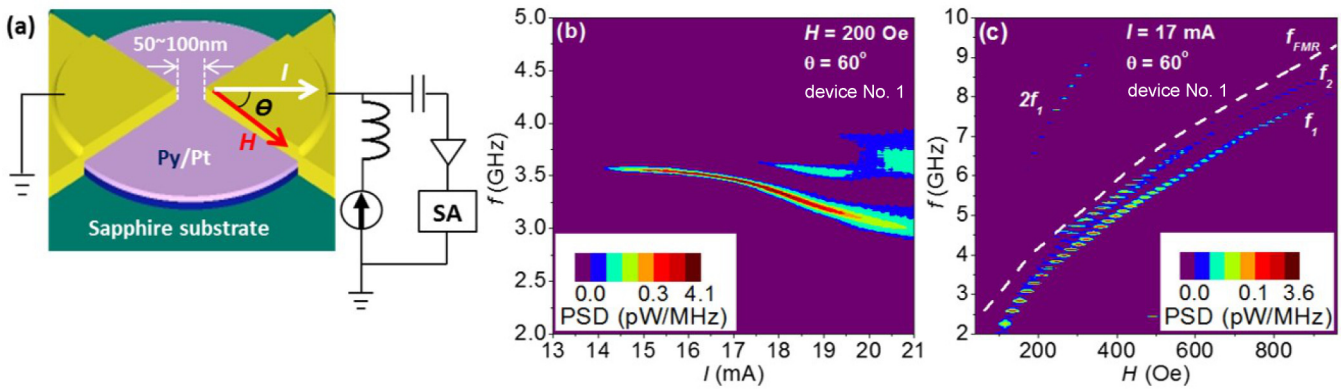


FIG. 1. (a) Schematic of the SHNO device structure and the experimental setup. (b), (c) Microwave generation characteristics of nanogap SHNO based on a Py(5)/Pt(4) bilayer, labeled device No. 1, with magnetic field $H$ oriented at 60° with respect to the current direction. (b) Pseudocolor map of the power spectral density (PSD) of the generated microwave signal, for current $I$ varying between 13 and 21 mA increased in 0.2 mA steps, at $H = 200$ Oe forming an angle $\theta = 60°$ with respect to the current direction. (c) Pseudocolor map of PSD obtained at $H$ between 40 and 960 Oe, $I = 17$ mA, and $\theta = 60°$. The dashed curve shows the ferromagnetic resonance (FMR) frequency $f_{\rm FMR}$ of the device, obtained using the spin-torque-driven FMR (ST-FMR) technique.

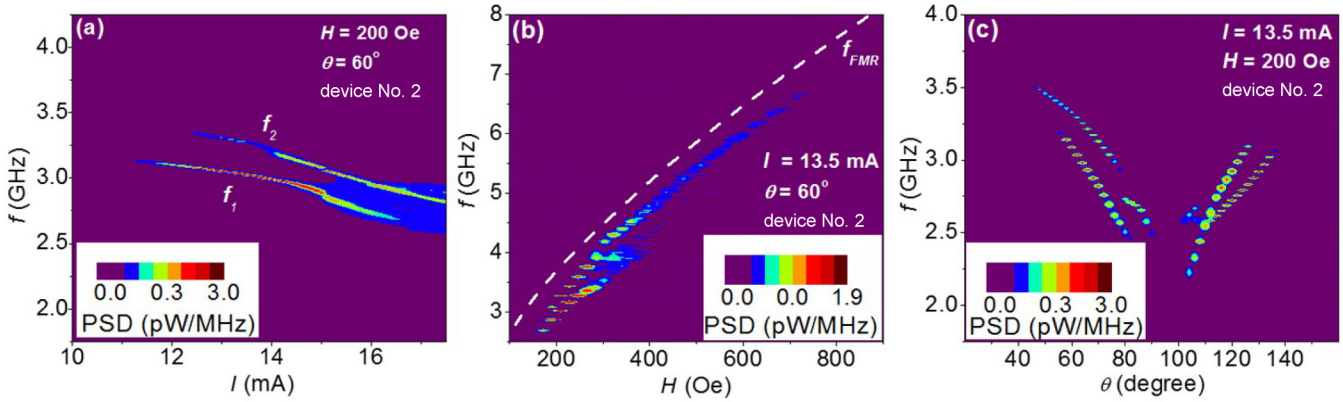


FIG. 2. Dependence of the microwave generation characteristics of nanogap SHNO based on a Py(3)/Pt(2) bilayer, labeled as device No. 2 on current $I$, magnetic field $H$, and its angle $\theta$ relative to the current flow. (a) Pseudocolor map of the spectra obtained at $H = 200$ Oe, $\theta = 60^\circ$, and $I$ varied from 10 to 17.5 mA in 0.2 mA increments. (b) Pseudocolor map of the spectra obtained at $I = 13.5$ mA, $\theta = 60^\circ$, and $H$ varied from 100 to 900 Oe. The dashed curve shows $f_{\mathrm{FMR}}$ for this device determined by the ST-FMR technique. (c) Pseudocolor map of the spectra obtained at $\theta$ varied between 30° and 150°, at $I = 13.5$ mA and $H = 200$ Oe.

(PSD) generated by the SHNO device No. 1, at field $H = 200$ Oe oriented at angle $\theta = 60^\circ$ relative to the current flow. A single mode was observed at the auto-oscillation onset at $I = 14.2$ mA, with the central frequency of $f_1 = 3.52$ GHz significantly below the FMR) frequency $f_{\mathrm{FMR}} = 4.1$ GHz of the Py(5)/Pt(4) film determined by the spin-torque FMR (ST-FMR) technique [35]. The frequency of the oscillation peak exhibited a small redshift with increasing current $I$, while its intensity increased until another peak with a higher frequency $f_2 = 3.6$ GHz appeared at $I = 17.6$ mA. The intensity of the higher-frequency peak increased with current in the range 17.6 mA to 19.6 mA, correlated with the decrease of the intensity of the low-frequency peak and its stronger redshift. Above 19.6 mA, the spectra exhibited two very broad peaks, indicating a transition to a new dynamical regime.

We gain insight into the nature of the observed modes by analyzing the dependence of the generation spectrum on the applied magnetic field $H$, at a constant current $I = 17$ mA, Fig. 1(c). The dashed line shows the FMR frequency $f_{\mathrm{FMR}}$ determined for the same device by ST-FMR. These data demonstrate that the frequency of the low-frequency mode remains far below $f_{\mathrm{FMR}}$ at all fields. We note that a peak at the second harmonic $2f_1$ of this mode emerges at fields between 200 and 400 Oe, indicating a large amplitude of the magnetization dynamics. Based on these data, as well as the results of previous BLS measurements and micromagnetic simulations [14,29], this mode can be identified as the self-localized spin-wave "bullet" [32]. The secondary higher-frequency mode emerges at fields above 280 Oe. Its frequency is only slightly below $f_{\mathrm{FMR}}$ at small fields, falling further below $f_{\mathrm{FMR}}$ at fields above 500 Oe. The nature of this mode is discussed below.

To determine whether the behaviors discussed above are the general features of SHNO or are specific to device No. 1, we analyzed the spectral characteristics of two additional SHNOs with a different thicknesses of the ferromagnetic layer. Figure 2 shows the microwave generation characteristics for device No. 2 based on the Py(3)/Pt(2) bilayer with Py thickness close to half of that in device No. 1. Figure 2(a) shows the dependence of the generated spectra on current, at $H = 200$ Oe and $\theta = 60^\circ$. The primary low-frequency mode appears above 11.2 mA, followed by the emergence of a secondary peak at 12.5 mA, and finally by a transition at 15 mA to the regime characterized by very broad peaks. These behaviors are consistent with those of device No. 1. Note that the onset of the secondary mode does not result in the broadening of the primary peak, indicating that the two modes coexist. The dependence on fields obtained at $I = 13.5$ mA and $\theta = 60^\circ$ shows that both $f_1$ and $f_2$ are below $f_{\mathrm{FMR}}$, also consistent with the data for device No. 1.

### C. Angular dependence of spectral characteristics

To further explore the relationship between the observed dynamical modes and the experimental parameters, we analyze the dependence of the generation spectra on the in-plane angle $\theta$ formed by the applied field relative to the direction of the current flow. The main trend in the dependence shown in Fig. 2(c) is a strong decrease of the peak frequencies when the angle approaches $\theta = 90^\circ$. By the symmetry of SHE, the maximum excitation efficiency, achieved when the magnetic moment carried by the spin current injected into Py is antiparallel to its magnetization, corresponds to $\theta = 90^\circ$. Therefore, the observed frequency decrease toward $\theta = 90^\circ$ is consistent with the strong nonlinear mode redshift due to the increasing excitation efficiency, in agreement with the dependence on current in Fig. 2(a). Oersted field of the current may also contribute to the frequency decrease. However, calculations (see Fig. 4 below) show that the component of Oersted field opposite to the applied field increases only by 10 Oe when $\theta$ is increased from 60° to 90°, accounting for the frequency decrease by only 0.05 GHz. We also note that the peaks vanish at $\theta$ close to 90°. Since the microwave signal is generated due to the AMR of Py [36], magnetization oscillation cannot generate a signal at the fundamental harmonic of oscillation at angles close to 90°. However, if the observed peaks corresponded to the second harmonic of oscillation, their intensity would not be expected to diminish at angles close to 90°. Thus, we conclude that all the peaks in Fig. 2(c) correspond to the fundamental harmonics of the excited dynamical modes.

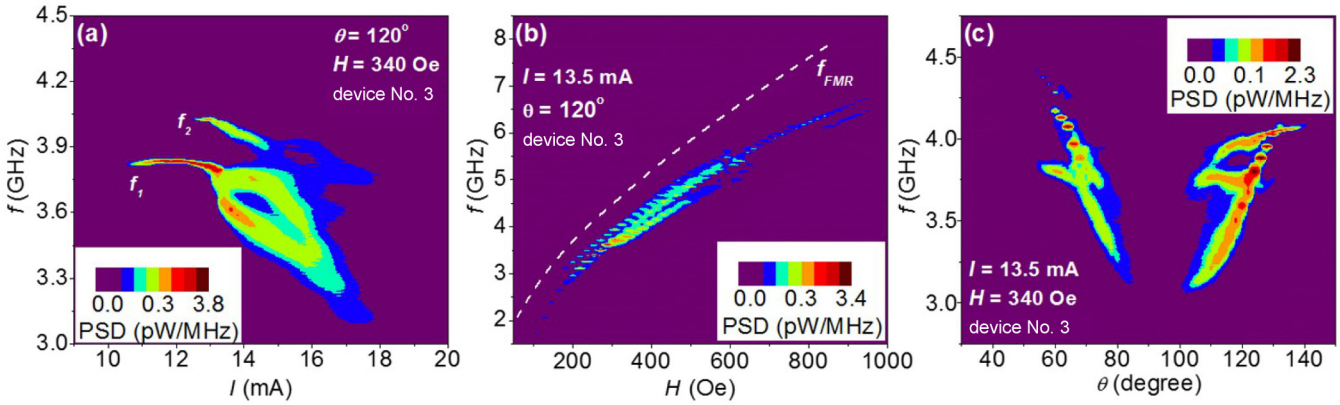


FIG. 3. Dependence of the microwave generation characteristics of nanogap SHNO based on a Py(3)/Pt(2) bilayer, labeled as device No. 3, on current $I$, magnetic field $H$, and its angle $\theta$ relative to the current flow. (a) Pseudocolor map of the spectra obtained at $I$ between 9 and 20 mA increased in 0.2 mA steps, $H = 340$ Oe, and $\theta = 120°$. (b) Pseudocolor map of the spectra obtained at $H$ varied between 40 and 1000 Oe, $I = 13.5$ mA and $\theta = 120°$. The dashed curve shows $f_{\mathrm{FMR}}$ of the device determined by the ST-FMR technique. (c) Pseudocolor map of the spectra obtained with $\theta$ varied between 30° and 150°, at $I = 13.5$ mA and $H = 340$ Oe.

For an ideal device depicted in Fig. 1(a), the effects of spin current are expected to be maximized at $\theta = 90°$, and then become symmetrically gradually reduced away from this angle. The measured angular dependence, shown in Fig. 2(c), exhibits overall trends that are symmetric with respect to $\theta = 90°$, but the specific spectral characteristics are somewhat asymmetric. The asymmetry can be explained by the device imperfections that result in a slightly asymmetric current flow. When coupled with the current-induced Oersted field, this breaks the symmetry between two otherwise equivalent field directions $\theta = 90° - \epsilon$ and $\theta = 90° + \epsilon$. Thus, the observed asymmetry demonstrates that the Oersted field provides a non-negligible contribution to the observed dynamics.

Devices No. 1 and No. 2 exhibit several common spectral features, such as sequential excitation of the primary and the secondary modes with increasing current, and transition to complex dynamical regime at high current, but their specific dynamical characteristics are somewhat different. To conclusively separate the general spectral features from device-specific details, Fig. 3 shows the same measurements as in Fig. 2, for device No. 3 with the same bilayer structure as device No. 2. The current- and field-dependencies for device No. 3 [Figs. 3(a) and 3(b)] exhibit the same general features as for devices No. 1 and No. 2, including the sequential onset of the two dominant modes at frequencies that are always below $f_{\mathrm{FMR}}$, and broad spectral features at large currents indicative of complex dynamics. The spectra also exhibit a strong angular dependence characterized by the same general trends as for device No. 2 [Fig. 3(c)]. The asymmetry with respect to $\theta = 90°$ is noticeably quantitatively different compared to device No. 2, confirming its origin from device imperfections.

## III. SIMULATIONS

### A. Oersted field and Joule heating effects

To elucidate the nature of the observed dynamical states, we performed micromagnetic simulations using the OOMMF software [37]. The simulation cell size was $5 \times 5 \times 3$ nm$^3$, and the simulated volume was a circular Py disk with the diameter of 1000 nm and thickness of 3 nm. To minimize the parasitic effects of spin-wave reflections from the boundary of the simulated disk, whose diameter is significantly smaller than that in our experiments, a highly absorbing boundary was used with the damping constant $\alpha = 1$. The following material parameters were used in the simulations: exchange stiffness $A = 13$ pJ/m, saturation magnetization $M_s = 800$ kA/m, Gilbert damping constant $\alpha = 0.04$, and spin Hall efficiency $P = 0.08$. The latter is defined as the ratio of spin current density injected into Py to the electron particle current density in Pt.

Figure 4 shows the current distribution in the Py(3)/Pt(2) device, as well as the resulting Oersted field and Joule heating in Py, which were numerically calculated with the COMSOL MULTIPHYSICS package [38] using the resistivity of 0.27 $\mu\Omega * m$ for the Py layer and 0.25 $\mu\Omega * m$ for the Pt layer. The current is strongly localized in the gap region [Fig. 4(a)]. The cross section of the current distribution through the center of the device, Fig. 4(b), shows that the current is localized mostly in the region of width 200 nm around the nanogap.

Our experimental results indicate that Oersted field $H_{\mathrm{Oe}}$ of the current significantly influences the observed dynamics [see Figs. 2(c), 3(c), and their discussions]. To account for these effects, position-dependent Oersted field was calculated from the current density distribution, and its contribution was taken into account in the micromagnetic simulations. Figure 4(c) shows a representative map of the spatial distribution of the total static external magnetic field $H_{\mathrm{Ext}}$, which includes the contributions of the applied in-plane field $H = 200$ Oe and the Oersted field $H_{\mathrm{Oe}}$ of the current $I = 11$ mA. In contrast to SHNOs based on Ta or W characterized by the negative spin Hall angle [39,40], the current-induced Oersted field $H_{\mathrm{Oe}}$ in Pt-based SHNO is opposite to the applied field. Figure 4(d) shows the profile of the in-plane component $H_{\mathrm{in\text{-}Ext}}$ of the total external field in the Py layer, in the cross-section through the middle of the gap aligned with the applied field, as indicated by the dashed line in Fig. 4(c). The magnitude of $H_{\mathrm{in\text{-}Ext}}$ is significantly reduced at the center of the gap, where current density is the largest.

To analyze the current-induced Joule heating effects, the spatial profile of the temperature of the active device area was also calculated using the COMSOL MULTIPHYSICS software

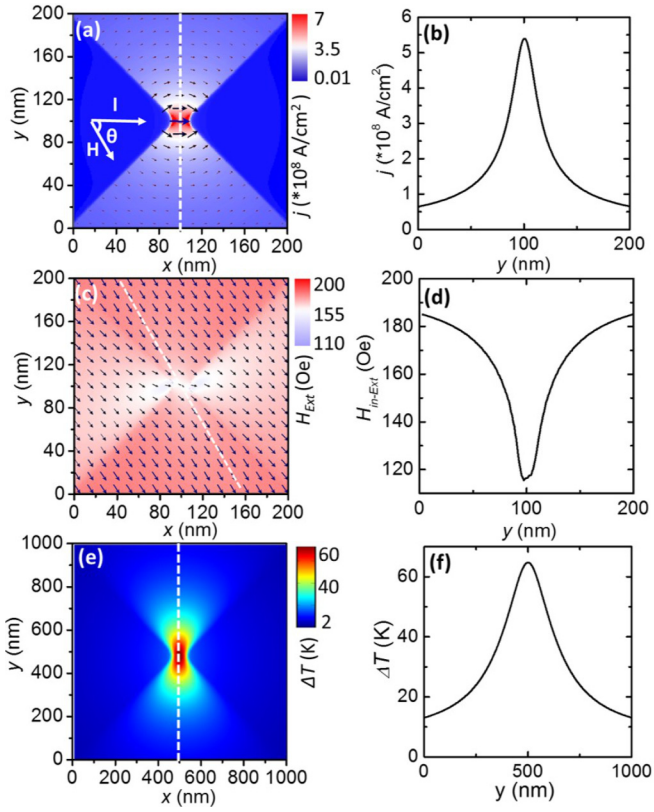


FIG. 4. Analysis of the distribution of current, Joule heating and the total external magnetic field in SHNO. (a) Calculated spatial map of the electrical current density in the Pt layer of device No. 2 with 80-nm gap between the Au electrodes, at $I = 14$ mA. (b) Section of the calculated current distribution along the $y$ axis transverse to the current flow [dashed line in panel (a)]. (c) Calculated spatial map of the total external magnetic field $\mathbf{H}_{\text{Ext}} = \mathbf{H}_{\text{App}} + \mathbf{H}_{\text{Oe}}$ in the Py layer of the device, at $I = 14$ mA, $H = 200$ Oe and $\theta = 60^\circ$. (d) Calculated amplitude of the in-plane component of $\mathbf{H}_{\text{Ext}}$ along the section shown in (c) with a dashed line, forming a 60° angle with the $x$ axis. (e) Calculated spatial map of temperature in the Py layer, at $I = 14$ mA. (f) Section of the temperature distribution along the $y$ axis transverse to the current flow, as shown by a dashed line in panel (e).

[38]. Figure 4(e) shows that the temperature of the Py layer is locally increased in the center region of the device. The cross section of the temperature distribution through the center of the device along the $y$ axis perpendicular to the current flow exhibits a maximum of about 70 K at the center of nanogap [Fig. 4(f)]. This result is consistent with the value of 60 K for the temperature of the active device area, inferred by comparing the $R$ vs $I$ and the $R$ vs $T$ curves. In addition, based on our previous studies of temperature-dependent spectra of SHNO [15,41], the bullet mode exhibits almost temperature-independent spectral characteristics at T < 150 K, except for the rescaling of characteristic excitation currents due to the varied efficiency of SHE. Therefore, we conclude that the temperature increase of the active device region caused by local Joule heating (not really localization compared to the size of bullet mode) is not expected to have a significant influence on the observed dynamical behaviors at the experimental temperature of 6 K. Therefore, in our micromagnetic simulations we have neglected the local heating effects.

### B. Dependence of power spectra on current and the direction of magnetic field

Micromagnetic simulations of current-induced magnetization dynamics based on the calculated total field and current distributions reproduced the general experimental observations common to the three studied devices, as illustrated by the dependence of spectra on current calculated at $H = 200$ Oe, $\theta = 120^\circ$ [Fig. 5(a)]. The primary low-frequency mode $f_1$ appeared first, followed by the onset at a moderately larger current of the secondary mode with a higher frequency $f_2$, and finally a transition to a broad spectral distribution at large currents. These results are consistent with the experimental observations. The two modes coexist in the calculated dynamics, also in agreement with our analysis of the data. The second and the third harmonics of the primary mode appeared in the calculated spectra at sufficiently large currents, due to the large amplitude of oscillation. These features are illustrated by the spectrum obtained at $I = 14$ mA, Fig. 5(b). The second harmonic of the primary mode $f_1$ was indeed experimentally observed for sample No. 1, Fig. 1(c). Higher-order harmonics (or even the second harmonic in samples No. 2 and No. 3) were not experimentally observed, likely due to the nonlinear damping effects, not captured by the simulations, that limited the oscillation amplitude.

The dependence of the calculated spectra on the orientation of in-plane field provides further evidence that the nonlinear effects are not fully captured by the simulations. Figure 6 shows the power spectra of $m_x$ obtained at $H = 200$ Oe for two different values of current. At a smaller current $I = 10$ mA [Fig. 6(a)], only the bullet mode is excited. Its frequency decreases when the field angle approaches $\theta = 90^\circ$. At larger current $I = 14$ mA, the calculated angular dependence of the bullet mode frequency becomes stronger, and the secondary modes is also excited [Fig. 6(b)]. While these results are qualitatively consistent with the experimental data, they underestimate the observed redshift toward $\theta = 90^\circ$, confirming our hypothesis that the micromagnetic simulations do not fully account for the nonlinear dynamical mechanisms. This limitation may be associated with the short-wavelength spin-wave cutoff by the finite simulation cell size. The significance of the contribution of short-wavelength THz spin waves to spin current-driven magnetization dynamics was recently inferred from the analysis of current-induced effects at low temperatures [42].

### C. Spatial characteristics of the auto-oscillation modes

The simulations provided insight into the spatial characteristics of the observed dynamical states and the mechanisms controlling their formation. Frequency-dependent maps of the dynamical magnetization were obtained by performing pointwise temporal FFT over the area of the Py disk. Figures 5(c)–5(l) show the normalized spatial power maps calculated from the time dependence of the local magnetization components $m_x$ and $m_z$, at the frequencies of the fundamental harmonics $f_1$ and $f_2$ of the two modes, as well as the second ($2f_1$) and the

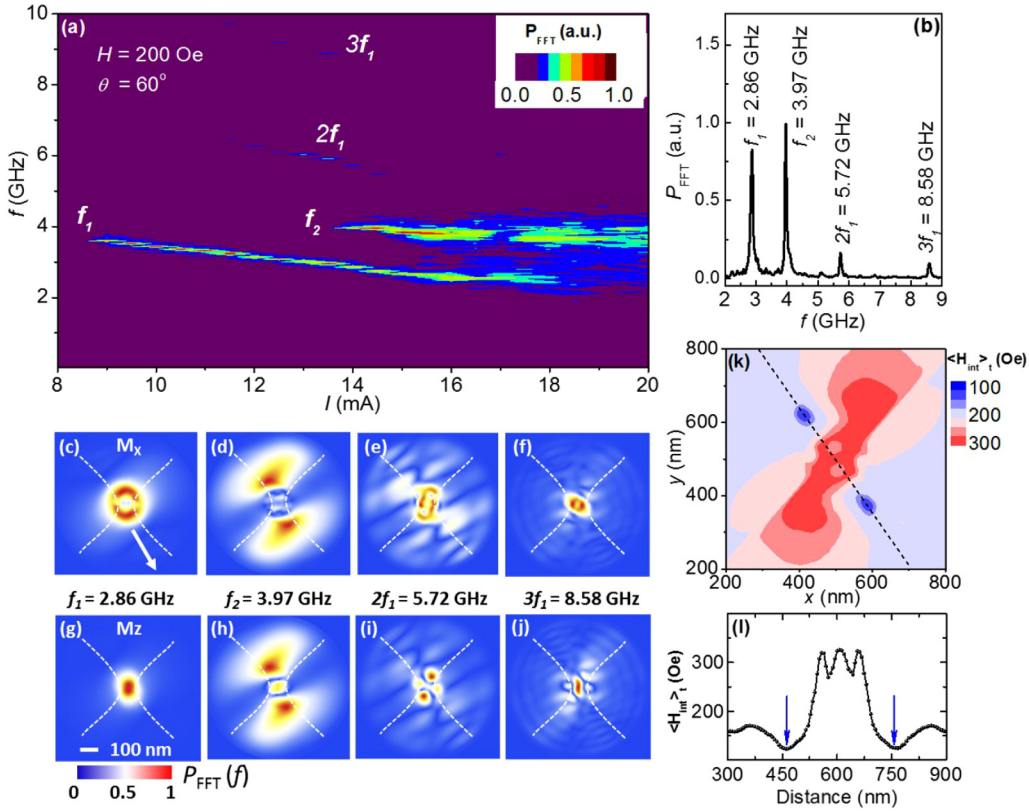


FIG. 5. Results of micromagnetic simulations for a Py(3) disk, in the configuration similar to that used in our measurements of devices No. 2 and No. 3, at $H = 200$ Oe and $\theta = 60°$. (a) Pseudocolor map of the simulated PSD as a function of applied current. (b) Representative auto-oscillation spectrum obtained at $I = 14$ mA. (c)–(f) Normalized spatial maps of the square of in-plane dynamical magnetization component $m_x^2$ corresponding to the two dominant auto-oscillation modes at $f_1 = 2.84$ GHz and $f_2 = 3.97$ GHz, as well as the second and the third harmonics of the primary mode at frequencies $2f_1 = 5.72$ GHz and $3f_1 = 8.58$ GHz, respectively. (g)–(j) Same as (c)–(g), for the square of the out-of-plane dynamical magnetization component $m_z^2$. Dashed lines show the contours of the electrodes, the arrow shows the direction of the applied field $H$, the scale bar is 100 nm. (k) Spatial map of the total time-averaged internal field $\langle H_{\rm int}\rangle_t$ determined at $H = 200$ Oe and $I = 14$ mA, which includes the applied and the Oersted field contributions, as well as the time-averaged dipolar field of the primary mode. (l) Section of $\langle H_{\rm int}\rangle_t$ along the direction of the applied field, as indicated by the dashed line in panel (k). The positions of the minima of the internal magnetic field are marked by two arrows.

third ($3f_1$) harmonics of the primary mode. The primary mode with the frequency $f_1$ far below $f_{\rm FMR}$ is localized in the region of about 100 nm at the center of gap, with approximately elliptical shape elongated in the direction perpendicular to the field. These characteristics are consistent with the prior BLS measurements and published simulations of the nonlinear self-localized spin-wave bullet [14,29]. We emphasize that the localization mechanism for this mode is qualitatively different from the localization by perturbations such as local dipolar fields produced by patterning of the magnetic layers or by the magnetic tips of scanning probes [43]. In particular, in contrast to these linearly localized modes, the bullet does not exist in the dynamical spectrum at any currents below the auto-oscillation threshold. The bullet mode abruptly spontaneously appears in the spectrum only at currents above the auto-oscillation threshold, with the spatial and the spectral characteristics determined not by the geometry of spin-current injection, but rather by the dynamical nonlinearity of the magnetic film [14]. The profile of the secondary mode with the frequency $f_2$ is characterized by two maxima offset from the center of the gap in two opposite directions collinear with the applied field, consistent with prior simulations performed at $\theta = 90°$ [29]. Our results demonstrate that the spatial characteristics of both modes can be efficiently controlled by the orientation of the magnetic field.

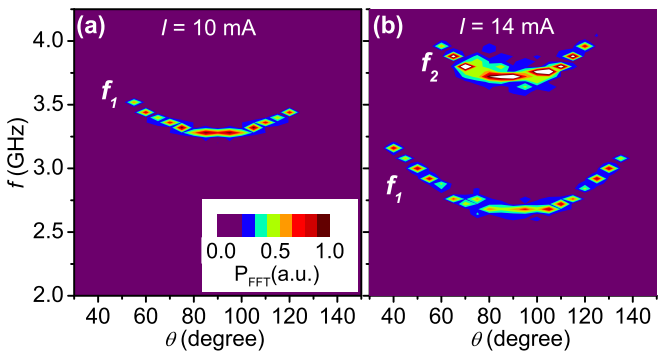


FIG. 6. Pseudocolor map of the simulated power spectra of $m_x$ for a Py(3) disk as a function of the angle $\theta$ of external in-plane magnetic field $H = 200$ Oe, at $I = 10$ mA (a), and 14 mA (b).

The secondary mode appears in the experimental spectra [Figs. 1–3] when the intensity of the primary mode becomes

large. Since the two modes coexist, one can expect that the perturbation produced by the primary mode dynamics substantially affects the characteristics of the secondary mode. To analyze this effect, we calculated the time-averaged internal magnetic field $\langle H_{\rm int}\rangle_t$ that includes the applied field $H_{\rm App}$, the Oersted field $H_{\rm Oe}$, and the time-averaged dipolar contribution of the dynamical magnetization associated with the bullet-mode precession, as shown in Figs. 5(k) and 5(l). The time-averaged internal magnetic field exhibits two local minima, offset from the device center in two opposite directions collinear with the applied field $H_{\rm App}$ [Figs. 5(k)–5(l)]. These minima arise due to the dipolar field produced by the bullet mode. The spatial profile of the secondary mode [Figs. 5(d) and 5(h)] exhibits a clear correlation with the location of these minima, indicating that it is stabilized by the spatially inhomogeneous dipolar field of the bullet mode. By comparing Figs. 5(c) and 5(d), we conclude that at moderate currents the spatial overlap of the two modes is very small, enabling their coexistence.

The maps of the second harmonic [Figs. 5(e) and 5(i)] and the third harmonic [Figs. 5(f) and 5(j)] of the primary mode provide insight into the mechanisms of the dynamic damping of auto oscillation. The frequencies $2f_1$, $3f_1$ of these harmonics are above $f_{\rm FMR}$, within the linear spectrum of propagating spin waves. Therefore, the local magnetization dynamics at these frequencies, associated with the bullet-mode precession, can be expected to couple to propagating spin waves at the corresponding frequencies. Indeed, the maps of these harmonics show intensity modulations consistent with spin-wave radiation from the active device region. This result reveals a previously unrecognized radiative contribution to the bullet-mode relaxation, originating from the nonlinear upconversion into propagating spin waves at the higher-order harmonics of the auto-oscillation frequency. It may be possible to utilize this mechanism of spin-wave radiation for spin-wave-mediated mutual synchronization of localized dynamical modes in SHNO.

### D. Chaotic dynamics

We now analyze the complex dynamics that emerges at large currents, as manifested by the broad spectral features observed both in the experiments [Figs. 1–3] and in simulations [Fig. 5(a)]. Figure 7(a) shows two time traces of the normalized magnetization component $m_z$ obtained at $I =$ 17.5 mA over the simulation time $t =$ 80–800 ns, with slightly different initial conditions at $t = 0$. The delay of 80 ns between the start of the simulation and the recorded trace eliminated the transient effects of the initial conditions. Both time traces exhibit similar oscillatory behaviors characterized by large amplitude variations. These variations are clearly not correlated between the two traces, suggesting that the magnetization dynamics is sensitive to the initial conditions. This observation is supported by the analysis of the fast Fourier transform (FFT) power spectra of these traces, Fig. 7(b). There is no quantitative correlation between the two spectra, aside from the overall two-peak structure retained from the two-mode oscillation at smaller currents. The sensitivity of both time domain and spectral characteristics to the initial conditions provides strong evidence for chaotic magnetization dynamics [44].

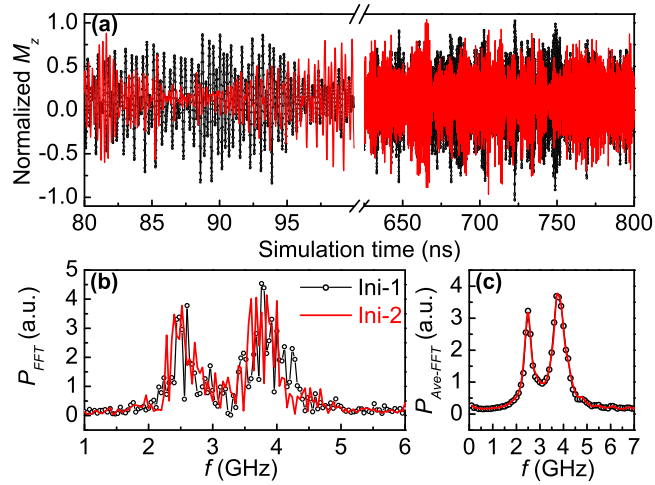


FIG. 7. Chaotic dynamics in the multimodal regime at $I =$ 17.5 mA and $H = 200$ Oe. (a) Time dependence of the normalized magnetization component $m_z$, for two slightly different initial states. (b) FFT power spectra of $m_z(t)$ obtained from the data in (a). (c) Average of 79 FFT power spectra obtained by dividing the data in panel (a) into sequential time windows of 10 ns width each. The results are shown by a solid curve for one of the data sets, and by symbols connected by lines for another.

The nature of this dynamics is elucidated by averaging the FFT power spectra of the time traces of $m_z$(t) broken up into 79 consecutive 10 ns-long intervals. The average spectra are identical for the two time traces [Fig. 7(c)]. They exhibit two well-defined peaks that can be traced to the two dominant dynamical modes discussed above. Thus, chaotic dynamics is likely associated with incoherent dynamical coupling between the two modes. Chaotic dynamics was predicted and observed experimentally in magnetic nano-oscillators dynamically coupled via electromagnetic interactions or external electrical circuits [44–47]. However, to the best of our knowledge, our results represent the first tentative observation of chaotic magnetization dynamics associated with incoherent dynamical coupling between two modes in a single nano-oscillator. Such chaotic dynamics belongs to the class of dissipative quadratic nonlinear systems that exhibit chaotic dynamics near their saddle equilibrium points of bi- or multistable energy landscape. High-speed chaotic dynamics associated with rapid incoherent switching between precession modes, accompanied by complex transients, may find applications in emergent information processing approaches such as chaos-based computing [48].

The simulations discussed above suggest the possibility of enhanced nonlinear coupling between the two modes at large currents, enabling rapid energy transfer between the two modes leading to chaotic dynamics. Superficially, these results seem to be inconsistent with the lack of correlation between the frequency evolution of the two modes at smaller currents, both in experimental measurements [Figs. 1(b), 2(a), 3(a)] and in simulations [Fig. 5(a)]. This apparent discrepancy can be resolved by analyzing the mechanism of the formation and the coupling between the two modes. The secondary mode is formed due to the dipolar minima produced by the primary mode, and experiences competing effects of the dynamical

dipolar and exchange fields of the primary mode. If only one of these effects was dominant, then the modes would synchronize, i.e., a single mode with a different profile would be formed. Thus, the existence of the secondary mode with a frequency different from the primary one is possible thanks to the balance of competing contributions to its interactions with the primary mode. However, as the amplitudes of the modes increase and/or they experience sufficiently strong fluctuations of their spatial profile, this balance becomes unstable, resulting in rapid transfer of energy between the modes. Further experiments and modeling are needed to clarify the complex nonlinear multimode dynamics in this regime.

## IV. CONCLUSION

To summarize, we utilized microwave spectroscopy and micromagnetic simulations to show that planar nanogap SHNOs based on in-plane magnetized extended magnetic films generally exhibit single-mode dynamics at small currents, two distinct coexisting modes at intermediate currents, and complex dynamics characterized by broad spectral features at large currents. The primary low-frequency mode was identified as a spin-wave bullet self-localized at the center of the device. The secondary mode is characterized by two maxima offset from the center of the device in two directions collinear with the field. Our simulations indicate that the coexistence of the two modes is facilitated by their small spatial overlap. We also identify a previously unrecognized dynamical mode relaxation mechanism of SHNO, due to the upconversion of the oscillation into a propagating spin wave at the higher-order harmonics of the oscillation. This mechanism can be utilized in the applications of SHNO as local spin-wave sources [49] and for synchronization of localized dynamical states in SHNO via propagating spin waves. Finally, our simulations suggest that the broad spectral features observed at large currents are associated with chaotic magnetization dynamics, originating from incoherent dynamic coupling between the primary bullet and the secondary modes. These results suggest several possibilities for applications of SHNO. For instance, the coexistence of two distinct modes suggests the possibility to implement logical operations based on the nonlinear coupling between these modes, while the chaotic dynamics observed at large currents can provide a practical platform for information processing via analog and neuromorphic computing [48,50,51].

## ACKNOWLEDGMENTS

L.C., Y.W.D, and R.H.L are supported by the National Key Research and Development Program of China (Grant No. 2016YFA0300803), National Natural Science Foundation of China (Grant No. 11774150), and Shenzhen Basic Research Program (Grant No. JCYJ20170818110402776). S.U. acknowledges support from NSF Grants No. ECCS-1804198 and No. DMR-1504449.

[1] J. C. Slonczewski, J. Magn. Magn. Mater. **159**, L1 (1996); **195**, L261 (1999).
[2] L. Berger, Phys. Rev. B **54**, 9353 (1996); J. Appl. Phys. **90**, 4632 (2001).
[3] M. Tsoi, A. G. M. Jansen, J. Bass, W.-C. Chiang, V. Tsoi, and P. Wyder, Nature (London) **406**, 46 (2000).
[4] S. I. Kiselev, J. C. Sankey, I. N. Krivorotov, N. C. Emley, R. J. Schoelkopf, R. A. Buhrman, and D. C. Ralph, Nature (London) **425**, 380 (2003).
[5] K. Ando, S. Takahashi, K. Harii, K. Sasage, J. Ieda, S. Maekawa, and E. Saitoh, Phys. Rev. Lett. **101**, 036601 (2008).
[6] V. E. Demidov, S. Urazhdin, E. R. J. Edwards, M. D. Stiles, R. D. McMichael, and S. O. Demokritov, Phys. Rev. Lett. **107**, 107204 (2011).
[7] I. M. Miron, K. Garello, G. Gaudin, P. J. Zermatten, M. V. Costache, S. Auffret, S. Bandiera, B. Rodmacq, A. Schuhl, and P. Gambardella, Nature (London) **476**, 189 (2011).
[8] T. Suzuki, S. Fukami, N. Ishiwata, M. Yamanouchi, S. Ikeda, N. Kasai, and H. Ohno, Appl. Phys. Lett. **98**, 142505 (2011).
[9] L. Liu, O. J. Lee, T. J. Gudmundsen, D. C. Ralph, and R. A. Buhrman, Phys. Rev. Lett. **109**, 096602 (2012).
[10] Z. H. Wang, Y. Y. Sun, M. Z. Wu, V. Tiberkevich, and A. Slavin, Phys. Rev. Lett. **107**, 146602 (2011).
[11] M. Collet, X. de Milly, O. d'Allivy Kelly, V. V. Naletov, R. Bernard, P. Bortolotti, J. Ben Youssef, V. E. Demidov, S. O. Demokritov, J. L. Prieto, M. Munoz, V. Cros, A. Anane, G. de Loubens, and O. Klein, Nat. Commun. **7**, 10377 (2016).
[12] M. B. Jungfleisch, W. Zhang, J. Sklenar, J. Ding, W. Jiang, H. Chang, F. Y. Fradin, J. E. Pearson, J. B. Ketterson, V. Novosad, M. Wu, and A. Hoffmann, Phys. Rev. Lett. **116**, 057601 (2016).
[13] W. Han, Y. Otani, and S. Maekawa, npj Quantum Mater. **3**, 27 (2018).
[14] V. E. Demidov, S. Urazhdin, H. Ulrichs, V. Tiberkevich, A. Slavin, D. Baither, G. Schmitz, and S. O. Demokritov, Nat. Mater. **11**, 1028 (2012).
[15] R. H. Liu, W. L. Lim, and S. Urazhdin, Phys. Rev. Lett. **110**, 147601 (2013).
[16] A. Zholud and S. Urazhdin, Appl. Phys. Lett. **105**, 112404 (2014).
[17] V. E. Demidov, H. Ulrichs, S. O. Demokritov, S. V. Gurevich, V. Tiberkevich, A. Slavin, A. Zholud, and S. Urazhdin, Nat. Commun. **5**, 3179 (2014).
[18] M. Ranjbar, P. Dürrenfeld, M. Haidar, E. Iacocca, M. Balinskiy, T. Q. Le, M. Fazlali, A. Houshang, A. Awad, R. K. Dumas, and J. Åkerman, IEEE Magn. Lett. **5**, 3000504 (2014).
[19] R. H. Liu, W. L. Lim, and S. Urazhdin, Phys. Rev. Lett. **114**, 137201 (2015).
[20] R. H. Liu, Lina Chen, S. Urazhdin, and Y. W. Du, Phys. Rev. Appl. **8**, 021001 (2017).
[21] T. Chen, R. K. Dumas, A. Eklund, P. K. Muduli, A. Houshang, A. A. Awad, P. Dürrenfeld, B. G. Malm, A. Rusu, and J. Åkerman, Proc. IEEE **104**, 1919 (2016).
[22] V. E. Demidov, S. Urazhdin, G. de Loubens, O. Klein, V. Cros, A. Anane, and S. O. Demokritov, Phys. Rep. **673**, 1 (2017).

[23] V. E. Demidov, S. Urazhdin, A. Zholud, A. V. Sadovnikov, and S. O. Demokritov, Appl. Phys. Lett. **105**, 172410 (2014).
[24] Z. Duan, A. Smith, L. Yang, B. Youngblood, J. Lindner, V. E. Demidov, S. O. Demokritov, and I. N. Krivorotov, Nat. Commun. **5**, 5616 (2014).
[25] H. Mazraati, S. Chung, A. Houshang, M. Dvornik, L. Piazza, F. Qejvanaj, S. Jiang, T. Q. Le, J. Weissenrieder, and J. Åkerman, Appl. Phys. Lett. **109**, 242402 (2016).
[26] A. A. Awad, P. Dürrenfeld, A. Houshang, M. Dvornik, E. Iacocca, R. K. Dumas, and J. Åkerman, Nat. Phys. **13**, 292 (2017).
[27] H. Mazraati, S. R. Etesami, Seyed Amir Hossein Banuazizi, S. Chung, A. Houshang, A. A. Awad, M. Dvornik, and J. Åkerman, Phys. Rev. Appl. **10**, 054017 (2018)
[28] T. M. Spicer, P. S. Keatley, M. Dvornik, T. H. J. Loughran, A. A. Awad, P. Dürrenfeld, A. Houshang, M. Ranjbar, J. Åkerman, V. V. Kruglyak, and R. J. Hicken, Appl. Phys. Lett. **113**, 192405 (2018).
[29] H. Ulrichs, V. E. Demidov, and S. O. Demokritov, Appl. Phys. Lett. **104**, 042407 (2014).
[30] T. Kendziorczyk and T. Kuhn, Phys. Rev. B **93**, 134413 (2016).
[31] M. Dvornik, A. A. Awad, and J. Akerman, Phys. Rev. Appl. **9**, 014017 (2018).
[32] A. Slavin and V. Tiberkevich, Phys. Rev. Lett. **95**, 237201 (2005).
[33] M. I. D'yakonov and V. I. Perel, JETP Lett. **13**, 467 (1971).
[34] J. E. Hirsch, Phys. Rev. Lett. **83**, 1834 (1999).
[35] J. C. Sankey, P. M. Braganca, A. G. F. Garcia, I. N. Krivorotov, R. A. Buhrman, and D. C. Ralph, Phys. Rev. Lett. **96**, 227601 (2006).
[36] T. McGuire and R. Potter, IEEE Trans. Magn. **11**, 1018 (1975).
[37] M. J. Donahue and D. G. Porter, OOMMF (NIST), http://math.nist.gov/oommf.
[38] COMSOL Multiphysics, COMSOL AB, Stockholm, Sweden. www.comsol.com.
[39] C.-F. Pai, L. Liu, Y. Li, H. W. Tseng, D. C. Ralph, and R. A. Buhrman, Appl. Phys. Lett. **101**, 122404 (2012).
[40] L. Liu, C.-F. Pai, Y. Li, H. W. Tseng, D. C. Ralph, and R. A. Buhrman, Science **336**, 555 (2012).
[41] Lina Chen, S. Urazhdin, Y. W. Du, and R. H. Liu, Phys. Rev. Appl. **11**, 064038 (2019).
[42] A. Zholud, R. Freeman, R. Cao, A. Srivastava, and S. Urazhdin, Phys. Rev. Lett. **119**, 257201 (2017).
[43] I. Lee, Y. Obukhov, G. Xiang, A. Hauser, F. Yang, P. Banerjee, D. V. Pelekhov, and P. C. Hammel, Nature (London) **466**, 845 (2010).
[44] Z. Yang, S. Zhang, and Y. C. Li, Phys. Rev. Lett. **99**, 134101 (2007).
[45] K. J. Lee, A. Deac, O. Redon, J. P. Nozieres, and B. Dieny, Nat. Mater. **3**, 877 (2004).
[46] X. A. Cheng, C. T. Boone, J. A. Zhu, and I. N. Krivorotov, Phys. Rev. Lett. **105**, 047202 (2010).
[47] S. Petit-Watelot, J.-V. Kim, A. Ruotolo, R. M. Otxoa, K. Bouzehouane, J. Grollier, A. Vansteenkiste, B. Van de Wiele, V. Cros, and T. Devolder, Nat. Phys. **8**, 682 (2012).
[48] R. Matsumoto, S. Lequeux, H. Imamura, and J. Grollier, Phys. Rev. Appl. **11**, 044093 (2019).
[49] B. Divinskiy, V. E. Demidov, S. Urazhdin, R. Freeman, A. B. Rinkevich, and S. O. Demokritov, Adv. Mater. **30**, 1802837 (2018).
[50] K. Yogendra, D. L. Fan, and K. Roy, IEEE Trans. Magn. **51**, 4003909 (2015).
[51] M. Romera, P. Talatchian, S. Tsunegi, F. A. Araujo, V. Cros, P. Bortolotti, J. Trastoy, K. Yakushiji, A. Fukushima, H. Kubota, S. Yuasa, M. Ernoult, D. Vodenicarevic, T. Hirtzlin, N. Locatelli, D. Querlioz, and J. Grollier, Nature (London) **563**, 230 (2018).